Laboratory investigation into the effect of the storage capacity of a city block on unsteady urban flood flows

Miguel Angel Mejía-morales, Emmanuel Mignot, André Paquier, Sébastien Proust

Laboratory investigation into the effect of the storage capacity of a city block on unsteady urban flood flows

Miguel Angel Mejía-Morales[1], Emmanuel Mignot[2], André Paquier[1], Sébastien Proust[1]

[1]INRAE - UR RiverLy, 5 rue de la Doua CS 20244 69625, Villeurbanne

[2]University of Lyon, LMFA, INSA Lyon, Ecole Centrale Lyon, Université Claude Bernard Lyon 1, 20 avenue A. Einstein 69621, Villeurbanne

Key Points:

- Access facilities to buildings and empty spaces within city blocks can modify the flood risk for the inhabitants of an urban area.
- The block storage capacity can reduce flow depths by up to 13% and increase velocities by up to 20% in the streets for the tested cases.
- The inflow hydrograph unsteadiness level has a strong influence on the floodwater volume stored in the block and thereby on the flood flows.

Corresponding author: Miguel Angel Mejía-Morales, miguel.a.mejia@outlook.com

This article has been accepted for publication and undergone full peer review but has not been through the copyediting, typesetting, pagination and proofreading process, which may lead to differences between this version and the Version of Record. Please cite this article as doi: 10.1029/2022WR032984.

Abstract

The increasing occurrence of urban flooding in recent years demands a more accurate flood hazard assessment. Therefore, a better understanding of the predominant hydraulic processes in urban flood flows is required. The present paper reports an experimental study conducted in a laboratory scale model, which represents an urban area consisting of a rectangular city block and four surrounding streets. The objective is to quantify the impact of open areas within the city block on the key features of floodwaters. Tests are carried out under unsteady flow conditions, by using three inflow hydrographs with different unsteadiness levels. For each inflow hydrograph, the space available for floodwater volume storage within the block (storage capacity, ϕ) is varied, keeping the boundary conditions unchanged. A case where the city block has no space for floodwater storage (i.e., $\phi = 0$) is used as a reference case. The results indicate that the unsteadiness level of the inflow hydrograph, especially during the rising stage, has a strong influence on the floodwater volume stored within the city block. The increase in storage capacity within the city block leads to a reduction of the global peak outflow discharge, a decrease in flow depths and a local increase in velocities in some streets and within the city block. Finally, with these variations in floodwater features, the level of risk to pedestrians is also impacted, increasing locally when the storage capacity of the block increases.

1 Introduction

In recent years, improving the understanding of urban flooding has become an extremely important issue, owing to the increasing occurrence of flooding events worldwide (more than twice in the last two decades compared to the previous two decades, according to CRED & UNDRR, 2020), and to the large number of affected people and the economic cost involved. Moreover, due to the influence of anthropogenic climate change on factors affecting flooding such as precipitation intensity and frequency, snow-melt and sea level, together with increasing extension of urban areas, it is projected that flash flooding and urban flooding may increase in the coming decades in several areas worldwide (Kundzewicz et al., 2014).

A better understanding of the urban flood processes also results in improved flood hazard and risk assessment. Flood hazard is typically related to parameters such as flow

depth (d) and velocity (U). Different methodologies have been developed based on these two parameters. The most common approach uses the product Ud, from which curves of hazard level are estimated. Hazard is assumed to be notable when the instability caused by the flood flow is initiated for a given target: either pedestrians (e.g., Abt et al., 1989; Karvonen et al., 2000; Cox et al., 2010), vehicles (e.g., Bonham & Hattersley, 1967; Gordon & Stone, 1973; Shu et al., 2011) or building (e.g., Black, 1975; Clausen & Clark, 1990; Milanesi et al., 2018).

Investigating urban flooding is a major challenge because of the high variability of flow patterns and the different constituents that interact with the flow, e.g., buildings, parked vehicles, street furniture and underground spaces. Thus, in an effort to improve flood hazard assessment in urban areas, recent studies have increasingly incorporated these complex flows (Mignot et al., 2019). Among all these constituents, buildings and their layout are the main feature of an urban environment. They are generally gathered in city blocks (the smallest group of buildings that is surrounded by streets), which can be considered as the elementary component that shapes an urban area. Besides buildings, city blocks can contain indoor open spaces such as parking lots, gardens and courtyards (Figure 1. a), as well as multiple vehicular and pedestrian access facilities, e.g., doors, gates and passageways (Figure 1.b), open or damaged during flooding. Therefore, city blocks are porous urban elements, and during a flood event the flow can be conveyed through a city block via these access facilities. Moreover, city blocks can also store floodwater volume, which can then modify the flood flow features in the nearby area.

During a flood event, a city block can then be characterized by: (i) its *conveyance porosity*, ψ, which allows the floodwater to be conveyed through the openings of the block sidewalls (see e.g., Meja-Morales et al., 2021); and (ii) its *storage capacity*, ϕ, which allows part of the floodwater volume to be stored within the block. Conveyance and storage characteristics have been commonly used when studying urban flooding based on 2D numerical modelling (e.g., Dottori & Todini, 2013; Bruwier et al., 2017; Ferrari et al., 2019). They have been used to define coefficients accounting for the effects that buildings or city blocks have on the flow: (i) the reduction of the volume available for storing water within the built-up area; (ii) the reduction of the section available for flow; and (iii) the energy loss induced by buildings acting as obstacles (Soares-Frazo et al., 2008). These coefficients have emerged in recent years, being applied in various manners, e.g., at the scale of the computational cells (e.g., Sanders et al., 2008) or at large-scale

Figure 1: a) Plan view of city blocks, showing the open interior space. b) Examples of gates and passages through city block walls for pedestrian and/or vehicular access. Images obtained from Google Maps.

as statistical descriptors (e.g. Soares-Frazo et al., 2008), dependent on the flow depth (e.g., zgen et al., 2016) or not (e.g., Guinot et al., 2017), etc. An extended recent review of these numerical models is provided by Dewals et al. (2021).

Therefore, the impact of buildings and/or city blocks on flood flows has been quite investigated in the last decades, mainly by using 2D numerical modelling (a review on building treatment and methodologies implemented in numerical modelling was provided, by Schubert & Sanders, 2012). However, most of the numerical developments were focused on the implementation of tools to simulate the effect of building blockage at large-scale, and for the sake of simplicity, most research works assumed that individual buildings or city blocks are non-porous elements (e.g. Mignot et al., 2006; Neal et al., 2009). Hence, in the literature on urban flooding, few papers took into consideration the effects of floodwater intrusion and storage within buildings or city blocks on the flow features. Note that, some research works have suggested to use spaces underneath buildings and city blocks as a flood mitigation measure. Among these, Avila et al. (2016), relying on 1D-2D numerical modelling, proposed the use of existing tanks underneath houses and buildings for the storage of runoff volume. The authors reported that by storing 3 - 17%

of this volume, the peak discharge can be reduced by 25 to 75% in the watershed under study.

During a flood event, the combined effects of non-porous buildings and porous buildings were investigated by Abdullah et al. (2011). They implemented an algorithm to filter LiDAR data, generating a Digital Terrain Model (DTM) that detected and classified buildings as impervious, with basements and with internal ground spaces. By applying this DTM in 1D/2D numerical modelling, they reported on average a 40% reduction in flow depths within the study area when incorporating this storage spaces in buildings, as well as a better agreement with recorded data from real-world flood events. Huang et al. (2014) also incorporated runoff storage in ground spaces within buildings in a 2D numerical model once the flood flow exceeded a defined threshold elevation. They concluded that the runoff volume storage in buildings reduced flow depths within the urban area, but that flash flooding could still cause major impacts in urban areas due to the rapidly increasing flow depth and fast flood propagation. Last, Paquier et al. (2019) studied the sensitivity of input parameters in 2D numerical modelling of urban flooding, including building treatment. They found that, by allowing runoff to be stored in the building-free areas within the city blocks, the maximum flow depth in the study area was hardly reduced ($< 1\%$), and the maximum velocity was reduced by only 5% compared to a simulation for which the city blocks were treated as non-porous elements. Thus, with the limited existing results no definitive conclusion can be drawn on the effect of internal storage areas on the flood flow features (flow depth, velocity, patterns).

In addition to numerical modelling, physical modelling is also a convenient option to study flooding in urban environments, especially for investigating complex flow patterns under controlled conditions (Finaud-Guyot et al., 2018). Moreover, due to the scarcity of reliable data available on real-world flood events, physical modelling can provide reference data for the validation and calibration of numerical models. However, in the literature on urban flooding, there are very few experimental studies focusing on the flood flow intrusion into buildings or city blocks, and all of them considered steady flow conditions, thus neglecting the *storage effect*. Among them, Mignot et al. (2020) studied the flow intrusion through various types of openings from a flooded street into an adjacent building. They found that the flow through the opening was strongly influenced by large objects (such as parked vehicles) located in the vicinity of the opening, and thus these objects should be taken into account for an accurate flood flow prediction. Meja-Morales

et al. (2021) studied the influence of flow exchanges between a porous city block and its surrounding streets on flow depths and velocities in the streets and block. They reported that an increase in the conveyance porosity of the block sidewalls can locally modify (increase or decrease with respect to a city block with no porosity) the flow depth and velocity by up to 12% and 70%, respectively, and subsequently influencing the flood risk to pedestrians based on the Ud product. Last, Li et al. (2021) investigated the influence of the building layout within a city block on flooding severity. They highlighted that the conveyance porosity in the dominant flow direction has a strong influence (locally increasing or decreasing) on velocities, flow depths and downstream discharge partition.

The present research work aims at quantifying the influence of the space available for water storage within a city block (in the horizontal plane) on the features of unsteady flood flows, varying the unsteadiness level of the inflow hydrograph. These experiments are conducted on a physical model termed Maquette Urbaine pour l'étude du Risque d'Inondation, MURI (Urban Model for the study of Flood Risk), focusing on a simplified rectangular city block and four surrounding streets. This simplified geometry puts aside the effects of a detailed topography on flow intrusion (as recently studied by Mignot et al., 2020), only focusing on the effect of the internal storage volume capacity of a city block with respect to the volume of the flood hydrograph and on the effect of the unsteadiness level of the flood hydrograph (rising and falling stages) on the local flood risk. The main objective is then to estimate the combined effects of a variable storage capacity of a porous city block and of a variable level of flow unsteadiness on flow depths, velocities and flow patterns in the streets and within the city block, as well as on the peak discharges in the street network.

Section 2 describes the experimental set-up, measurement techniques, and the studied flow cases (storage capacity values and inflow conditions). The experimental results are exposed in Section 3, particularly, the impact of the block storage capacity on the outflow discharges, flow depths and velocities, as well on the risk to pedestrians. Section 4 presents a discussion on the main findings, and the conclusions are drawn in Section 5.

2 Methodology

2.1 Experimental set-up

The experiments are carried out on the physical model MURI, located at the Hydraulics and Hydro-morphology Laboratory (HHLab) of INRAE, Villeurbanne, France. It is a tilting platform 5.4 m long and 3.8 m wide, which represents an urban district comprising three longitudinal streets and three transverse streets, bounding 16 city blocks (Figure 2.a). The model horizontal scale ratio is $\lambda_{xy} = 50$, thus it represents a prototype urban area of 270 m by 190 m. The present study is carried out in a reduced area of MURI. This experimental set-up focuses on a single city block (with a simplified geometry but still similar to those found in real downtown areas, such as those shown in Figure 1.a) connected to the surrounding streets (respectively labelled, upstream, downstream, right and left, see Figure 3.a) by an opening in each sidewall (a 6 cm wide rectangular opening representing an open gate, see Figure 2.b). Within the block, a non-porous building is placed (Figure2.b and Figure 3). Its planar area is increased to decrease the available storage capacity, ϕ. The width of each street is $b = 0.15$ m (7.5 m in the prototype), the rectangular city block is 1.56 m long and 0.96 m wide (78 m by 48 m in the prototype), made of 2 cm thick smooth plastic vertical walls (PMMA). The bed platform, made of PVC panels, is tilted in the longitudinal direction with a slope of $S_{0_x} = 0.12\%$ (aligned with the x-axis), while the slope in the transverse direction (aligned with the y-axis) is nil. The bed roughness height was estimated to $k_s = 3.6 \times 10^{-5}$ m. The flow circulation in the experimental facility is ensured by a pumping-loop system. Water enters the model through the inlet tank of the right street and is evacuated at the downstream end of each of the four streets (4 outlets) with free outflow conditions (Figure 3). These outlets are free (without weir) to avoid any wave reflection from the weir towards the street network under unsteady flow conditions, and to facilitate the evacuation of water between each repetition of the inflow hydrograph.

2.2 Measuring techniques

To characterize the flow patterns within the urban area, the data acquired combine flow depth and surface velocity measurements, along with simultaneous measurements of the inflow and outflow discharges. The measurement of each flow parameter is detailed below.

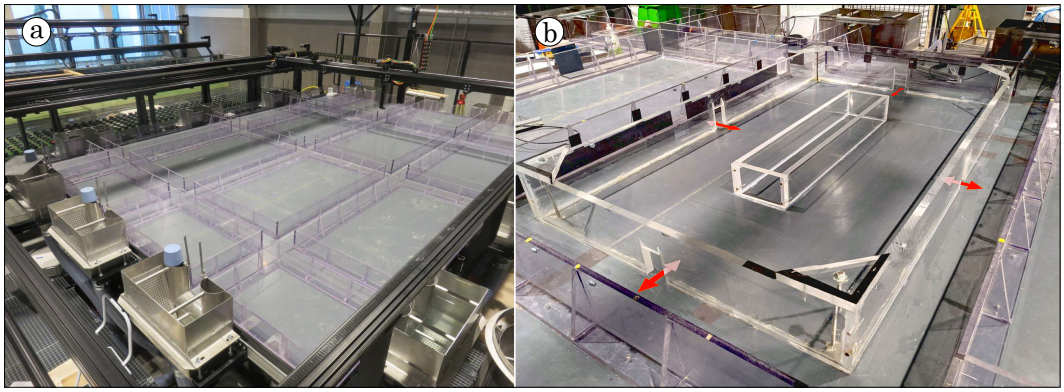

Figure 2: a) Overview of the Maquette Urbaine pour l'étude du Risque d'Inondation, MURI (Urban Model for the study of Flood Risk). b) Close-up of the city block with an opening in each of its sidewalls (conveyance porosity, ψ), including a non-porous inner building that reduces the space available for storing floodwater volume (storage capacity, ϕ). The red arrows stand for flow exchanges between the streets and the city block through the openings.

2.2.1 Discharge

The inflow discharge and each outflow discharge are measured with dedicated electromagnetic flowmeters (OPTIFLUX 2000 by KROHNE), whose accuracy is equal to 0.3% of the measured discharge, and which are capable of measuring a minimum discharge of 0.13 $\mathrm{l\,s^{-1}}$ (according to preliminary tests). The inflow discharge is regulated by a flow-measuring control system (valve-flowmeter system located along the inlet conduit, upstream of the inlet tank, as shown in Figure 3.a). This system permits steady or unsteady flows to be produced with a high degree of repeatability.

All discharge values presented in this study are *time-averaged values* for steady flows, and *ensemble-averaged values* for unsteady flows. To set the appropriate acquisition duration for the time-averaged discharge values, time convergence of the flowmeters signal is estimated by performing independent tests with discharges ranging from 0.2 to 5 $\mathrm{l\,s^{-1}}$ (where 0.2 $\mathrm{l\,s^{-1}}$ is very close to the minimum possible value that flowmeters are able to measure and 5 $\mathrm{l\,s^{-1}}$ is the maximum allowed in the inlet tanks to avoid overflows). Convergence is obtained when the acquisition duration is higher than 400 s at a sampling rate of 50 Hz (see section 1 in the Supporting Information for more details). For the unsteady flow experiments, an inflow hydrograph, controlled by the automatic electrovalve-

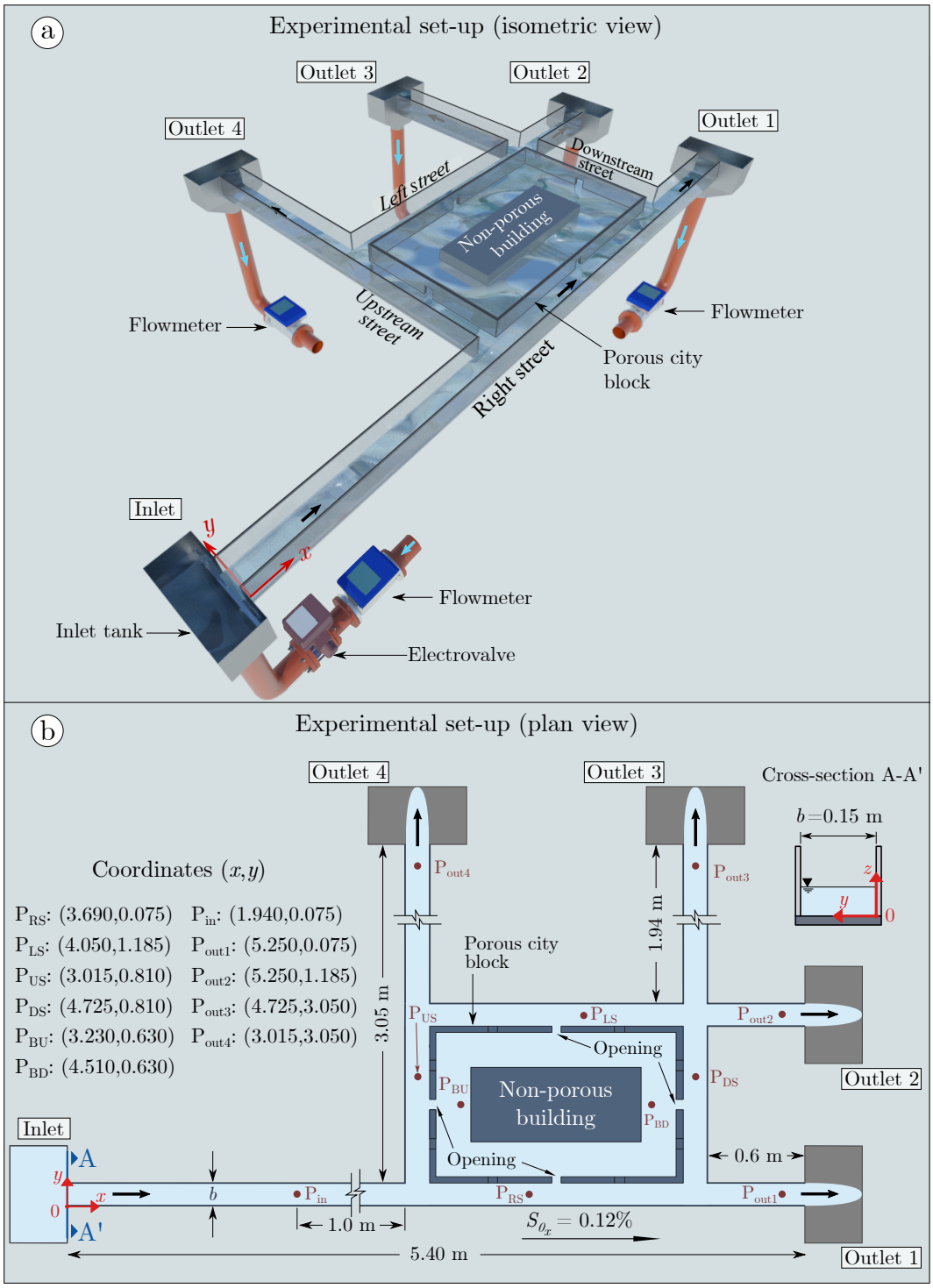

Figure 3: a) Isometric schematic of the experimental set-up. b) Schematic plan view of the experimental set-up, featuring all dimensions and locations of the measurement points: in the streets surrounding the block (P_{RS}, P_{LS}, P_{US}, P_{DS}), within the block (P_{BU}, P_{BD}), close to the outlets (P_{out1}, P_{out2}, P_{out3}, P_{out4}), and in the inlet street (P_{in}).

flowmeter system, is injected at the upstream end of the right street (Figure 3.a). To reach a converged ensemble-averaged inflow hydrograph, 50 replicates of the inflow hydrograph are required according to a convergence test performed (for details see section 2 in the Supporting Information).

2.2.2 Flow depth

Flow depths, d, are computed from the measurements of the bed and free-surface flow elevations using ultrasonic distance-measuring sensors (BAUMER UNDK 20I6914/S35A). Their accuracy is 0.3 mm (according to the manufacturer) and their reproducibility is on average 0.34 mm (based on eight independent flow depth measurements at ten different locations on the mesurement domain). The ultrasonic sensors were installed within the study area at various locations, denoted as: P_{RS}, P_{LS}, P_{US} and P_{DS} in the right, left, upstream and downstream streets, respectively; P_{out1}, P_{out2}, P_{out3} and P_{out4} at 15 cm upstream of the outlets 1, 2, 3 and 4, respectively; P_{in} in the inlet street; and P_{BU}, P_{BD} in the upstream and downstream zones within the block, respectively (Figure 3.b). The measurements are taken at a sampling rate of 50 Hz. The acquisition duration for the steady flow depths is 400 s, equal to the discharge acquisition duration. For the unsteady flows, the number of replicates of the stage hydrograph to reach a converged ensemble-averaged stage hydrograph is set to 50, as for the inflow hydrograph (see section 3 in the Supporting Information for more details).

2.2.3 Surface velocity

The two-dimensional (2D) surface velocity field, denoted as $U_s(x, y)$, is measured in the streets and within the block using the Large Scale Particle Image Velocimetry technique (LSPIV). Wood shavings with diameters ranging from 1 to 4 mm are released as free-surface tracers. A video camera is placed 2.2 m above the study area, with the optical axis perpendicular to the model bed. The spatial resolution of the camera is 1920×1080 px, and the recording rate is 25 frames per second. In addition to natural light, four led lamps with an adjustable light intensity are used along with light diffusion screens to light up the set-up. The free Fudaa-LSPIV software co-developed by EDF/INRAE (Le Coz et al., 2014) is used to process the videos and compute the surface velocities.

This technique is applied to both steady and unsteady flows. For steady flows, the recording duration of 60 s (i.e., 1500 consecutive images) allows to achieve convergence of the time-averaged velocity field, as proposed by Meja-Morales et al. (2021). For unsteady flows, an averaging time of 2 s corresponding to 50 consecutive images seems a good compromise between a high enough sampling frequency and an estimate of the average time-varying velocity field (see section 4 in the Supporting Information for more details).

2.3 Variable storage capacity

Within the city block, non-porous rectangular buildings (with smooth plastic sidewalls) of decreasing size are successively placed at the center of the city block (Figure 3.b) to increase the block storage capacity, ϕ, defined as:

$$\phi = \frac{A_B - A_b}{A_B} \tag{1}$$

where A_B is the total horizontal surface within the city block and A_b is the horizontal surface covered by the non-porous building.

Five different cases are considered, as depicted in Figure 4. First, a reference scenario, for which the city block is completely closed ($A_B = A_b$), i.e. storage capacity $\phi = 0$, and then $\psi = 0$ as well. Then, three non-porous rectangular buildings of different size are placed within the block, to vary the storage capacity. Their dimensions are 1.19 m $\times$ 0.59 m (for $\phi = 0.5$), 0.96 m $\times$ 0.36 m (for $\phi = 0.75$), and 0.78 m $\times$ 0.18 m (for $\phi = 0.90$). Last, the maximum possible storage capacity ($\phi = 1$) is obtained by keeping the city block empty. For all cases with non-zero storage capacity, the size and distribution of the openings in the city block sidewalls are unchanged (i.e. constant ψ-value).

2.4 Inflow conditions

Three different inflow hydrographs are considered (Figure 5.a). They have the same peak discharge ($Q_{pk} \approx 5$ l s^{-1}) but different features, i.e. the rising time, T_r, the falling time, T_f, and the total floodwater volume dispatched, V (Figure 5.b). For each feature the magnitude is either *Small* (denoted as S) or *Large* (denoted as L). These characteristics are shown on each inflow hydrograph label, the first, second and third letters after H corresponds to the magnitude of T_r, T_f and V. H.LSS thus refers to an inflow hy-

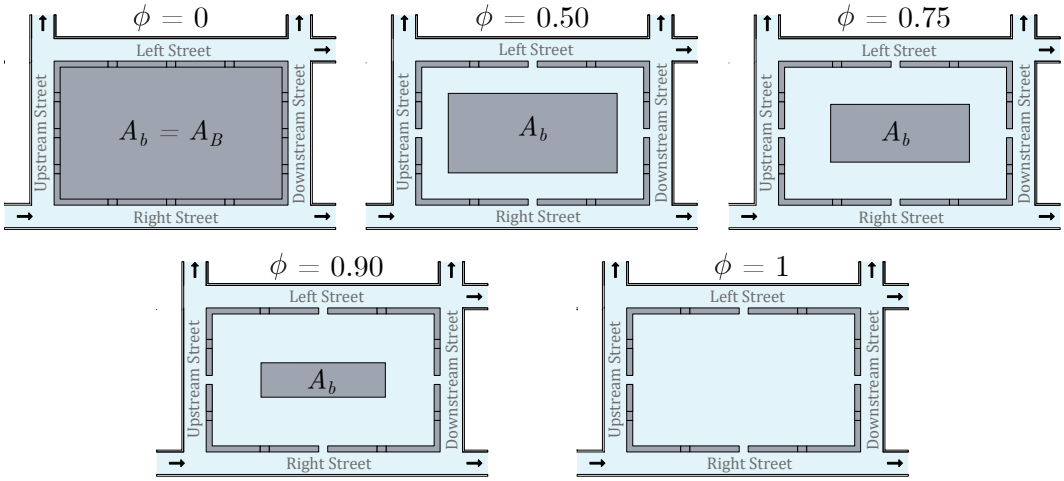

Figure 4: Variable storage capacity within the block, ϕ (Eq. 1). The case with $\phi = 0$ serves as the reference flow condition.

drograph with large T_r, small T_f and small V, and for the other two hydrographs, the label also shows the magnitude of each characteristic. All characteristics of the three inflow hydrographs are listed in Table 1. The values are averaged over the 50 hydrograph replicates (as explained in subsection 2.2.1), and are thus indicated with notation $\langle\,\rangle$.

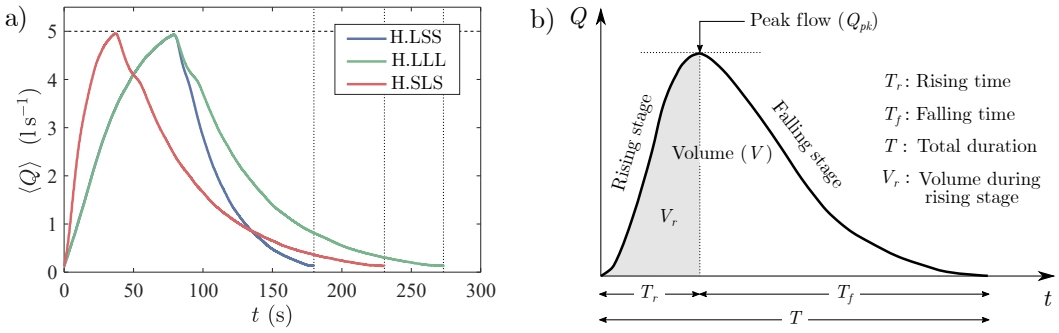

Figure 5: a) Inflow hydrographs considered, whose features are reported in Table 1. The minimum recorded discharge is 0.13 ls^{-1}, as explained in the subsection 2.2.1. b) Sketch of the inflow hydrograph characteristics reported in Table 1.

The unsteadiness level of each of the three inflow hydrographs is quantified using the parameter α proposed by Nezu and Nakagawa (1993), which involves the rising speed of the free-surface, S, and the convection velocity of turbulent eddies, U_c, defined as:

$$S = \frac{d_p - d_b}{T_r} \tag{2}$$

$$U_c = \frac{U_b + U_p}{2} \tag{3}$$

$$\alpha = \frac{S}{U_c} = \frac{2(d_p - d_b)}{T_r(U_b + U_p)} \tag{4}$$

where subscripts b and p refer to the base flow and peak flow, respectively (e.g., d_b is the base flow depth and d_p is the peak flow depth).

In the present work, no base flow is considered, thus the city block has no stored water before the begining of the inflow hydrograph. However, as an inflow hydrograph starts just at the end of the previous hydrograph, a residual volume remains in the experimental set-up between two hydrograph replicates and then, d_b is very small but not zero. Conversely, as the velocity of this residual volume is almost nil, it is considered that $U_b = 0$. For each inflow hydrograph, two values of the unsteadiness parameter are computed and reported in Table 1, one corresponding to the rising stage, α_r (computed with Eq. 4), and the other to the falling stage, α_f (replacing T_r by T_f in Eq. 4). These values are estimated at the measurement point $\mathrm{P_{in}}$ along the inlet street (Figure 3.b). For H.LSS and H.LLL, with the same T_r, α_r is quite similar ($\sim 2.2 \times 10^{-3}$), while for H.SLS, with a smaller T_r, α_r is higher and equal to 4.5×10^{-3}. The same analysis holds for α_f, which increases as T_f decreases.

In addition to unsteady flows, steady flows are also investigated with five inflow discharges, Q_{in}= 1, 2, 3, 4 and 5 $\mathrm{l\,s^{-1}}$, for comparison with the unsteady flow tests.

2.5 Distorted-scale model

To transfer the present results to the prototype scale, the vertical scale ratio, λ_z, is considered different from the horizontal scale ratio, with:

$$\lambda_{xy} = \frac{L_{xy_P}}{L_{xy_M}} = 50 \tag{5}$$

$$\lambda_z = \frac{L_{z_P}}{L_{z_M}} = 30 \tag{6}$$

where L_{xy} and L_z correspond to the dimensions in the horizontal plane (xy) and in the vertical direction (z), respectively, and subscripts M and P refer to the scale *Model* and the real-world *Prototype*, respectively. This difference in scale ratios allows for greater

Table 1: Characteristics of the inflow hydrographs, where Q_{pk} is the peak discharge, T_r is the rising time, T_f is the falling time, T is the total duration, V_r is the volume dispatched from $t = 0$ to $t = T_r$ (Figure 5.b), V is the total volume of the inflow hydrograph and α_r and α_f are the unsteadiness parameters (Eq. 4) for the rising and falling stages of the inflow hydrograph, respectively.

Inflow Hydrograph	$\langle Q_{pk} \rangle$ (l s^{-1})	$\langle T_r \rangle$ (s)	$\langle T_f \rangle$ (s)	$\langle T \rangle$ (s)	$\langle V_r \rangle$ (l)	$\langle V \rangle$ (l)	α_r $\times 10^{-3}$	α_f $\times 10^{-3}$
H.LSS	4.94	79.40	100.50	179.90	251.34	408.12	2.22	1.54
H.LLL	4.93	79.38	193.88	273.26	250.33	525.46	2.20	0.79
H.SLS	4.95	37.16	193.54	230.70	124.67	400.29	4.49	0.77

flow depths and Reynolds numbers in the model when simulating a real-world event, which is useful to improve measurements accuracy and the dynamic similarity to the prototype (Li et al., 2019).

Since the effects of the gravity force are predominant in free-surface flows, Froude similitude, i.e., $\mathrm{Fr}_M = \mathrm{Fr}_P$, permits to up-scale the values from the experimental model to the real-world prototype (Chanson, 2004). This implies for flow depth, velocity, discharge and time, the following ratios:

$$\frac{d_P}{d_M} = \lambda_z \tag{7}$$

$$\frac{U_P}{U_M} = \lambda_z^{1/2} \tag{8}$$

$$\frac{Q_P}{Q_M} = \lambda_z^{3/2} \lambda_{xy} \tag{9}$$

$$\frac{t_P}{t_M} = \lambda_z^{-1/2} \lambda_{xy} \tag{10}$$

Therefore, by up-scaling the dimensions of the experimental facility to the real-world dimensions, the city block is 78 m long by 48 m wide, with a 3 m wide opening through each of the four sidewalls. The characteristics of the different inflow hydrographs at the prototype scale are reported in Table 2.

Table 2: Characteristics of the inflow hydrographs at the *prototype scale*.

Inflow Hydrograph	$Q_{pk,P}$ ($m^3\ s^{-1}$)	$T_{r,P}$ (min)	$T_{f,P}$ (min)	T_P (min)	V_P (m^3)
H.LSS	40.50	12.08	15.29	27.37	30609
H.LLL	40.50	12.08	29.50	41.58	39426
H.SLS	40.67	5.65	29.45	35.10	30035

3 Results

3.1 Flow overview

For all unsteady flow tests, the flow remains subcritical most of the time in the left street (Fr ≈ 0.5), the maximum flow depth is 2.0 cm and the maximum surface velocity, U_s, is about 0.2 $\mathrm{m\,s^{-1}}$. Oppositely, in the the right street, the higher discharge leads to a supercritical flow regime most of the time (Fr ≈ 1.6), the surface velocity can reach 0.9 $\mathrm{m\,s^{-1}}$, and the maximum flow depth is $d \approx 3.0$ cm. The flow in the upstream and downstream streets goes from the right street to the left street. The difference in flow regime between the right and left streets generates hydraulic jumps both in the upstream and in the downstream streets, with a maximum value of $d \approx 2.0$ cm. Within the city block, free-surface is nearly horizontal most of the time (with a flow depth ranging between 1.6 and 2 cm, among all storage capacities and different inflow hydrographs), with the flow depth always being slightly higher in the upstream zone (at measuring point $\mathrm{P_{BU}}$, Figure 3.b) than in the downstream zone (at $\mathrm{P_{BD}}$) due to the longitudinal bed slope, S_{0_x}. Water mainly enters the block through the opening connected to the right street, and leaves it through the openings connected to the left and downstream streets.

The features of the steady flows are generally similar for some parameters to those described for the unsteady flows, with some noticeable differences for others that will be discussed in the following sections.

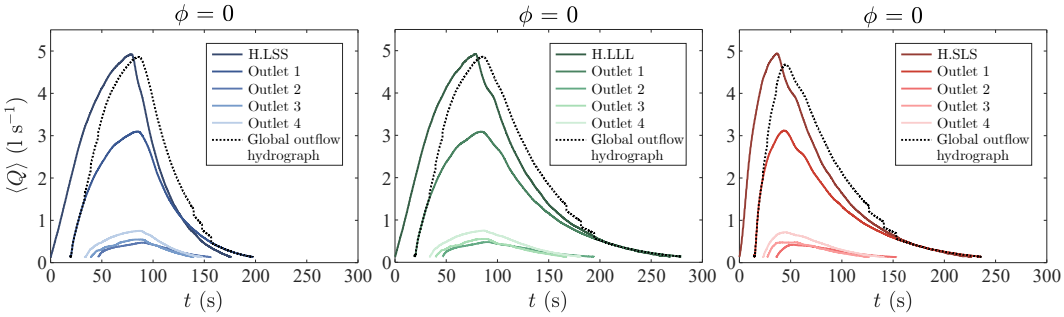

Figure 6: Inflow hydrographs (H.LSS, H.LLL and H.SLS), outflow hydrographs (outlets 1,2,3 and 4) and global outflow hydrographs, for the reference flows, i.e., $\phi = 0$.

3.2 Outflow discharges

The peak outflow discharges significantly differ among the four outlets (Figure 6), always being much greater at outlet 1 (right street), in the range of 61-66% of the total peak outflow discharge, $Q_{pk,out,tot}$, (Figure 7.a). The discharges through outlets 2 and 3 (left and downstream streets) are comparable, about 10%, and the discharge at outlet 4 (upstream street) ranges from 15 to 18% of the total peak outflow discharge.

Since the city block stores part of the floodwater volume (when $\phi \neq 0$), an attenuation of the peak discharge, Q_{pk}, in the outflow hydrographs is expected with respect to the reference scenario (with no storage capacity, i.e., $\phi = 0$). This is confirmed when the four outflow hydrographs (four outlets) are merged (added together by using the start of the inflow hydrograph as a reference point, see Figure 6) to constitute the global outflow hydrograph. Overall, increasing the storage capacity of the city block attenuates the peak discharge of the global outflow hydrograph, for the three inflow hydrographs, H.LSS, H.LLL and H.SLS (Figure 7.f). The maximum relative change occurs for H.SLS, where the peak discharge is reduced by 10% when $\phi = 1$. For the other two inflow hydrographs, with similar α_r, the peak discharge attenuation is similar, 5.9% and 5.2%, respectively.

When looking at each outflow hydrograph separately, the peak discharge attenuation is confirmed for the outflow hydrograph 1 (at outlet 1) for all storage capacity values (Figure 7.b), and also most of the storage capacity values for the outflow hydrograph 3 (Figure 7.d). However, flow exchanges between the city block and streets can increase the discharge in streets reaches where the exchange flow is directed from the block to

the street, as shown by Meja-Morales et al. (2021) and Li et al. (2021). This is the case for outflow hydrograph 4 (Figure 7.e), for which an increased peak discharge is observed, except for H.SLS, with the largest unsteadiness level, α_r. Consequently, the variations in the peak discharge are not only related to the storage capacity of the block (ϕ) and the conveyance porosity of its walls (ψ), but also to the different flow pathways resulting from the modification of the empty space within the block. This is supported by the results for the steady flow case with $Q_{in} = 5\,\mathrm{l\,s^{-1}}$ (circular markers in Figures 7.b to 7.e), for which there is no floodwater volume stored within the block (same discharge enters and leaves the block), but still some influence on the outflow discharges is observed when the space within the block is modified.

In addition, Figure 8 shows the relative change in time lag with respect to the reference case (denoted as Δt_L) for a variable ϕ. This lag is defined as the time difference between the peak discharges of the inflow and global outflow hydrographs. From $\phi = 0$ to $\phi = 0.5$, the time lag increases by $\sim$10% for the three inflow hydrographs, but it does not noticeably increase for larger ϕ values ($0.5 \leq \phi \leq 1$). Therefore, the relative increase in time lag seems to be mostly related to the conveyance of the flow through the city block openings (conveyance porosity, ψ), rather than the storage capacity, ϕ.

3.3 Flow depth

The storage capacity of the city block can strongly affect flow depths in the surrounding streets, as previously reported by Huang et al. (2014), but some particularities are found herein. In the right street, where the flow discharge is predominant, the relative change in maximum flow depth, d_{max}, (compared with the reference case) is lower than 4% (Figure 9.a). Conversely, in the left, upstream and downstream streets, this change is much more noticeable and it differs according to the inflow hydrograph unsteadiness parameter, α_r. For instance, for H.SLS, d_{max} always decreases (i.e., from $\phi = 0$ to $\phi = 1$), up to -13% in the left and downstream streets when $\phi = 1$ (Figures 9.b and 9.d). However, for H.LSS and H.LLL, d_{max} always increases from $\phi = 0$ to $\phi = 0.5$, and decreases as ϕ continues increasing (Figures 9.b, c and d). Therefore, for the latter two inflow hydrographs, the initial increase is related to the conveyance porosity, ψ, (same as for the steady flow $Q_{in} = 5\,\mathrm{l\,s^{-1}}$) and contrary to H.SLS, for most cases, d_{max} is always higher than in the reference case, up to 11% in the upstream street.

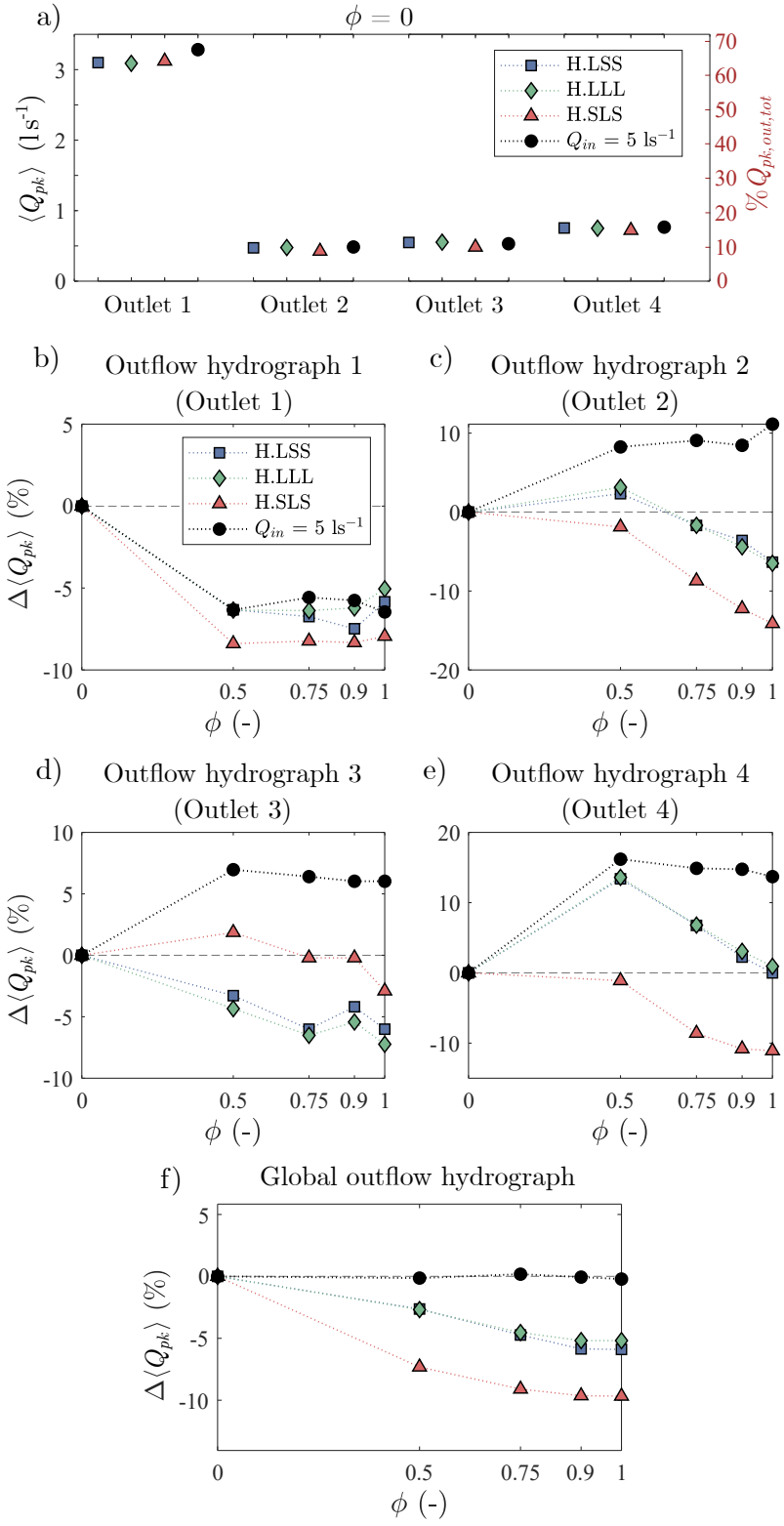

Figure 7: a) Peak discharge, $\langle Q_{pk} \rangle$, of each outflow hydrograph for the reference case (i.e., for $\phi = 0$). Relative change in peak discharge, $\Delta\langle Q_{pk} \rangle$, for each outflow hydrograph (b-e) and for the global outflow hydrograph (f) with respect to the reference case, as a function of the storage capacity, ϕ. Results are shown for the three inflow hydrographs (H.LSS, H.LLL and H.SLS) and for the steady flow case with $Q_{in} = 5\,\mathrm{ls}^{-1}$.

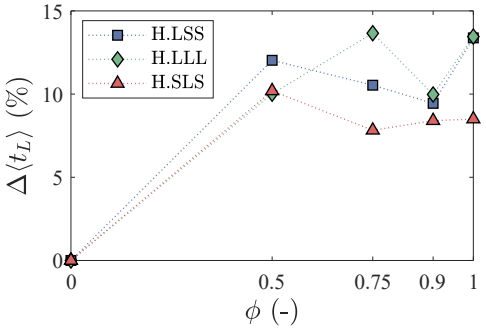

Figure 8: Relative change in time lag, $\Delta\langle t_L\rangle$, with respect to the reference case ($\phi = 0$), between the peak discharges of the inflow and global outflow hydrographs, as a function of the storage capacity of the city block, ϕ.

For the street reaches that are not adjacent to the block (inlet street and street reaches next to the outlets) the effect of storage capacity, ϕ, is reduced in most cases. The smallest effect is found in the inlet street (location P_{in}, Figure 3.b), where a maximum relative change with respect to the reference case is observed, about 4% (Figure 9.i). For the reaches next to the outlets, the influence of ϕ is slightly higher (Figures 9.e, f, g and h), mainly in the reach next to the outlet 4, with a maximum relative change of 10% compared to the reference case.

Within the city block, the flow depth is averaged between locations P_{BU} and P_{BD} (Figure 3.b). The maximum flow depth decreases when the storage capacity increases (Figure 10.a). Moreover, for the steady flow case, $Q_{in} = 5\ \mathrm{l\,s^{-1}}$, and for all ϕ values, the flow depths are greater than those observed in unsteady flows, up to 30% for the case with the maximum storage capacity ($\phi = 1$). Here, the evolution of the flow depth is again very similar for the inflow hydrographs H.LSS and H.LLL. This proves the significant influence of the rising stage unsteadiness parameter, α_r, on the flow depth within the block, and thus on the stored floodwater volume.

The maximum flow depths within the city block (Figure 10.a) permit to compute, the maximum floodwater volumes stored within the block, $V_{B,max}$, for the three inflow hydrographs and all storage capacity values. These values are normalised by the total volume dispatched by each inflow hydrograph, V (Figure 10.b). The largest, $V_{B,max}/V$ ratio, correspond to H.LSS, with 3.6% to 6% stored volume, which according to Figure 7.f, leads to a peak discharge attenuation between 3 and 6%. Nearly the same attenu-

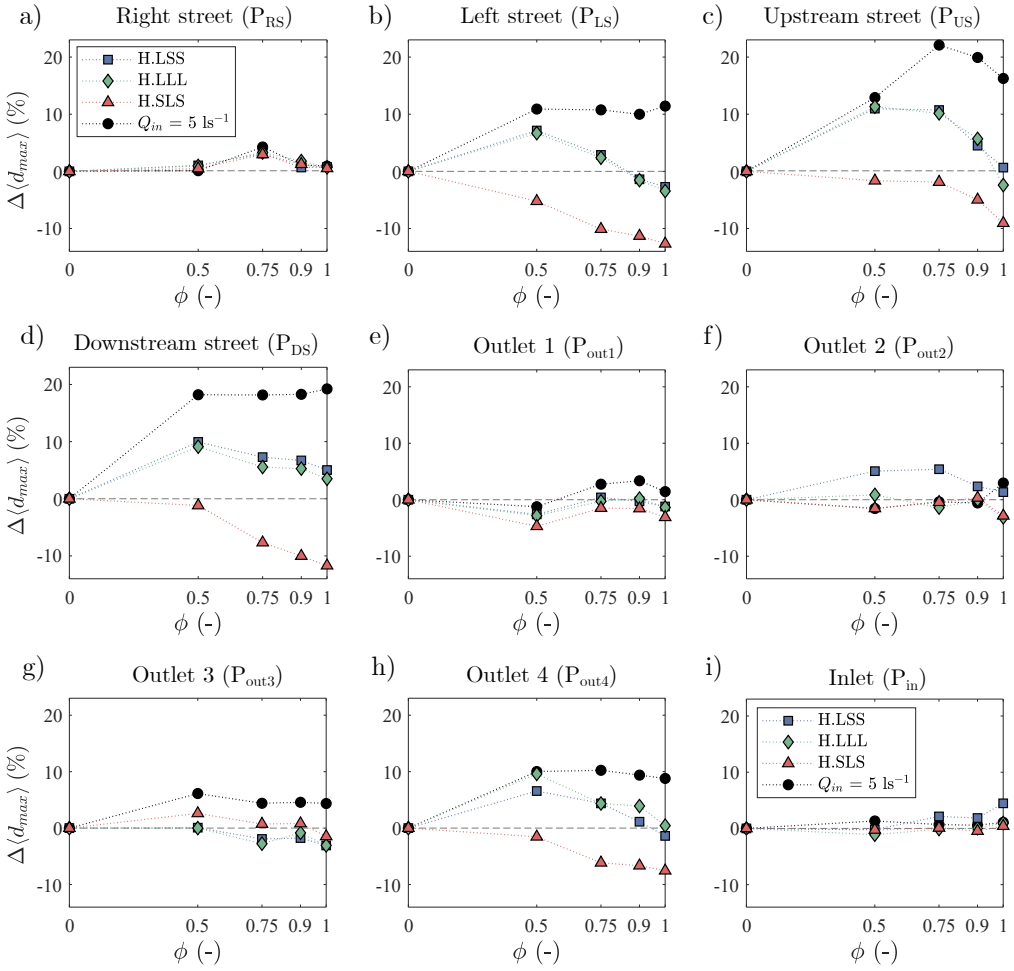

Figure 9: Relative change in maximum flow depth, $\Delta\langle d_{max}\rangle$, with respect to the reference scenario (d_{max} for $\phi = 0$) as a function of the storage porosity, for the three inflow hydrographs and the steady flow with $Q_{in} = 5$ ls^{-1}. The plots are shown for the street reaches surrounding the city block, at locations P_{RS} (a), P_{LS} (b), P_{US} (c) and P_{DS} (d) and for the street reaches not adjacent to the block, at locations P_{out1} (e), P_{out2} (f), P_{out3} (g), P_{out4} (h) and P_{in} (i), see Figure 3.b.

ation range is observed for H.LLL, but with a lower $V_{B,max}/V$ ratio (between 2.8% and 4.7%). Oppositely, normalising $V_{B,max}$ by the volume dispatched only during the rising stage, V_r (Figure10.c), exhibit similar $V_{B,max}/V_r$ ratios for these two inflow hydrographs (H.LSS and H.LLL), for all ϕ values. For H.SLS, the stored volume related to V_r is much greater than for the other two, by about 100%, which explains the higher peak discharge attenuation, and also the greatest influence on maximum flow depths, d_{max}, observed for this inflow hydrograph. Consequently, using V_r for normalising the stored volume seems more appropriate.

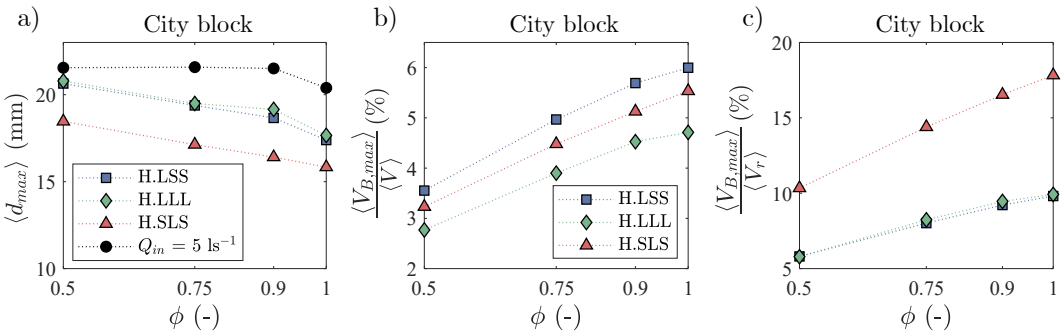

Figure 10: a) Maximum flow depth, d_{max}, within the city block (averaged between the two measurement points, P_{BU} and P_{BD}) as a function of the storage capacity, ϕ, for the three inflow hydrographs, and flow depth for the steady flow case with $Q_{in} = 5\,\mathrm{l\,s^{-1}}$. Maximum stored floodwater volume within the city block, $V_{B_{max}}$, as a function of the storage capacity, ϕ, for the three inflow hydrographs, normalised by the total floodwater volume dispatched by each inflow hydrograph, V, in b), and normalised by the floodwater volume dispatched during the rising stage, V_r, in c).

3.4 Surface velocities

For the unsteady tests with the inflow hydrograph H.LSS (for all ϕ values), the time evolution of the surface velocity field was only measured in the right and left streets[1] (at P_{RS} and P_{LS}, Figure 3.b) and within the city block.

[1] The presence of an oblique hydraulic jump, which moved along the street with the change in flow discharge, prevents from using the LSPIV technique to estimate velocities in the upstream and downstream streets.

In the right street, where the flow regime is supercritical in steady flow and during most of the unsteady flow, the maximum surface velocity is roughly the same for both steady and unsteady flows and hardly varies when ϕ increases (Figure 11.a). Compared to the reference case, the maximum variation in $U_{s,max}$ is about 2% (Figure 11.b). In the left street, the flow regime is subcritical and the maximum surface velocity for $\phi = 0$ is very similar for both steady and unsteady flows, 0.22 $\mathrm{m\,s^{-1}}$ and 0.21 $\mathrm{m\,s^{-1}}$, respectively (approximately 1/4 of the maximum velocity found on the right street), see Figure 11.a. Contrary to the right street, there is a strong variation in $U_{s,max}$ in the left street with respect to the reference case when ϕ increases. For the steady flow, this variation ranges from -30% to -20%, while for the unsteady flow it ranges from -9% to 10% when ϕ increases from 0.5 to 1 (Figure 11.b).

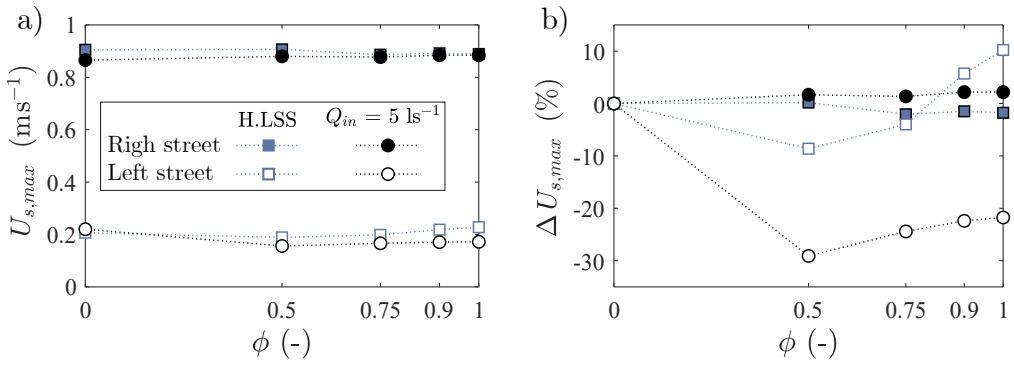

Figure 11: Maximum surface velocity, $U_{s,max}$ (a), and relative difference in maximum velocity, $\Delta U_{s,max}$ (b), with respect to the reference scenario ($\phi = 0$), as a function of the storage capacity of the city block, ϕ, in the right and left streets, for H.LSS and the steady flow case with $Q_{in} = 5\,\mathrm{l\,s^{-1}}$.

Within the city block, the magnitude of the time-varying surface velocity ranges from 0 to 0.33 $\mathrm{m\,s^{-1}}$. For each ϕ value (except for $\phi = 0$), five 2D surface velocity maps are plotted in Figure 12: two maps during the rising stage (identified by labels R50 and R75), one map at maximum flow depth, d_{max}, within the block (identified by the label P100) and two maps during the falling stage (identified by labels F50 and F75), see Figure 12. The numbers 50 and 75 refer to 50% and 75% of d_{max}, respectively. For all ϕ values, the velocities during the rising stage are greater than during the falling stage. Among all cases, the highest maximum velocity is obtained for $\phi = 1$, with a magnitude approximately 7% higher than for the other ϕ values. As the main intrusion flow into the block

occurs through the right street opening, the greatest velocities take place in this area. The water jet here, together with the clearance between the block walls and the non-porous building walls, have a great influence on the flow pattern and form a complex recirculating flow area with multiple large-scale cells. For $\phi = 0.5$, where the clearance is the smallest, up to ten recirculation cells are observed at R75. The number of recirculating cells then decreases with the enlargement of the clearance: eight cells for $\phi = 0.75$, seven cells for $\phi = 0.90$, and only five cells for $\phi = 1$ (three large and two small).

For the steady flows, the surface velocity magnitude ranges from 0 to 0.28 $\mathrm{m\,s^{-1}}$, with the maximum velocity reached for $\phi = 1$. An interesting finding is that the maximum velocity in steady flow is lower than in unsteady flow, for all ϕ values, by -15% to - 20%. The number of recirculation cells is also lower for the steady flow than for the unsteady flow (at P100), except for $\phi = 1$, where two main cells take place at the flood peak (P100) as in steady flow regime.

3.5 Flood risk at the prototype scale

The Froude similitude (Eqs. 7 and 8) permits to estimate the velocities and flow depths at the real-world prototype scale. We assume here that the surface velocity equals the depth-averaged velocity. This assumption is based on the measurements perfomed by Meja-Morales et al. (2021) on this same MURI model, under steady flow conditions. They showed that surface velocities obtained by the LSPIV technique are very similar to flow depth-averaged velocities measured with an ADV within the city block, are slightly underestimated in the left street (by 8%), and are overestimated in the centreline of right street (by 20%). Thus, the $U_s{-}d$ curves in the right and left streets, for steady (indicated with markers in grey tones) and unsteady flows (indicated by coloured dashed lines) for the various ϕ values are integrated in the flood risk diagram for pedestrians proposed by Meja-Morales et al. (2021), as shown in Figure 13. In the right street, the level of flood risk evolves from *low* to *high* during the rising stage and oppositely during the falling stage. The *high* risk level occurs during about 60% of the flood duration, mainly due to the elevated velocities measured in this street (Figure 11.a). The hysteresis, that is typical of unsteady flows in open channels, leads to a different level of risk during the rising and falling stages, mostly for flow depths below 0.5 m and velocities lower than 3 $\mathrm{m\,s^{-1}}$. For a given flow depth, the level of risk is always higher during the rising stage, while for a given velocity, the level of risk is always higher during the falling stage.

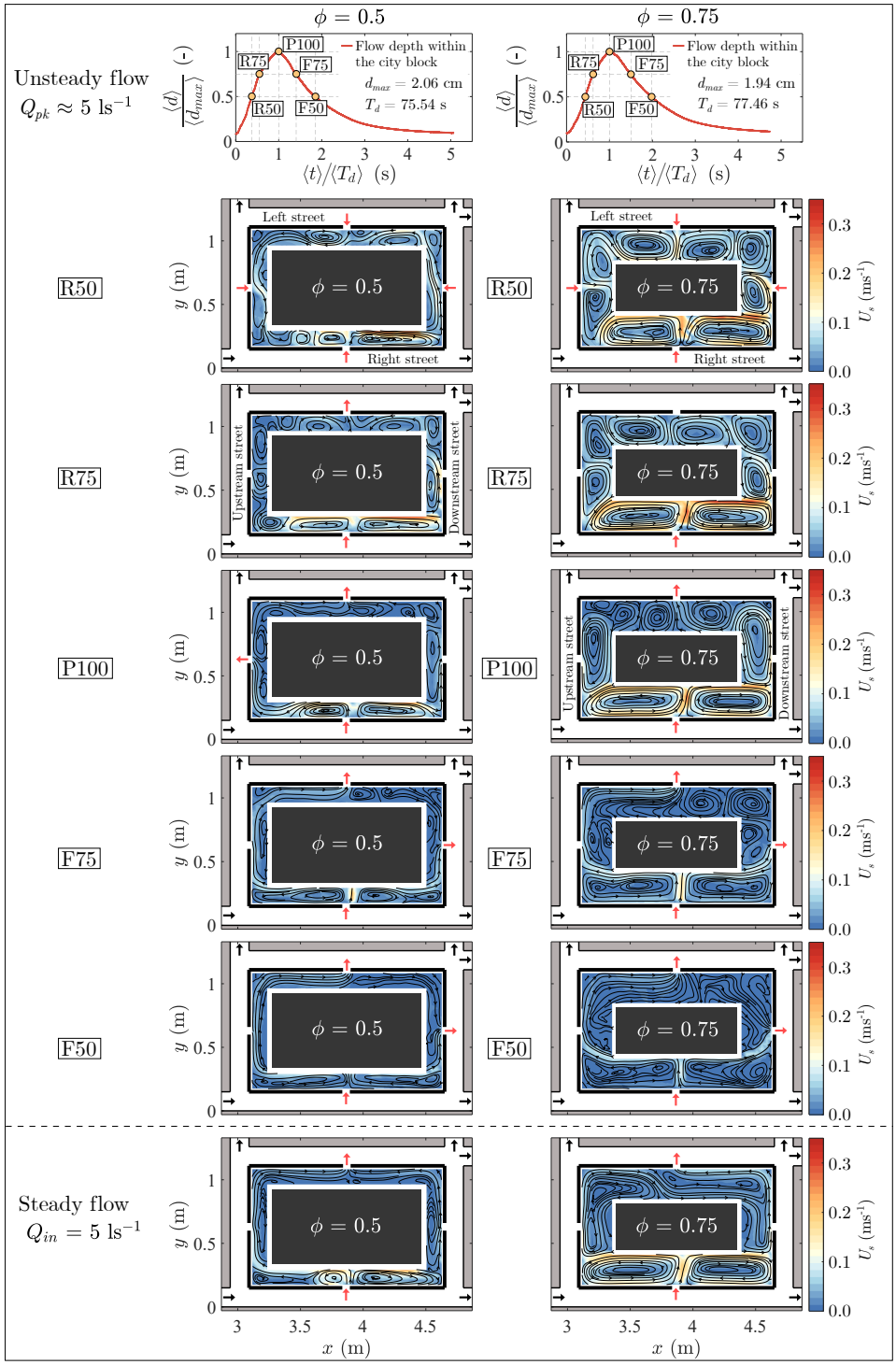

Figure 12: Surface velocity, U_s, within the city block for storage capacity values $\phi =$ 0.50, 0.75, 0.9 and 1 for unsteady flow (H.LSS), at five different instants: at 50% and 75% of d_{max}, during the rising stage (R50 and R75) and falling stage (F50 and F75), and at d_{max} (P100). For the steady flow with $Q_{in} = 5$ ls^{-1} the velocity map is shown at the bottom. Black arrows indicate the flow direction in the streets and red arrows through the openings in the block walls. At the top is shown the stage hydrograph, $d(t)$, within the city block, where T_d is the time between the base and maximum flow depths within the city block.

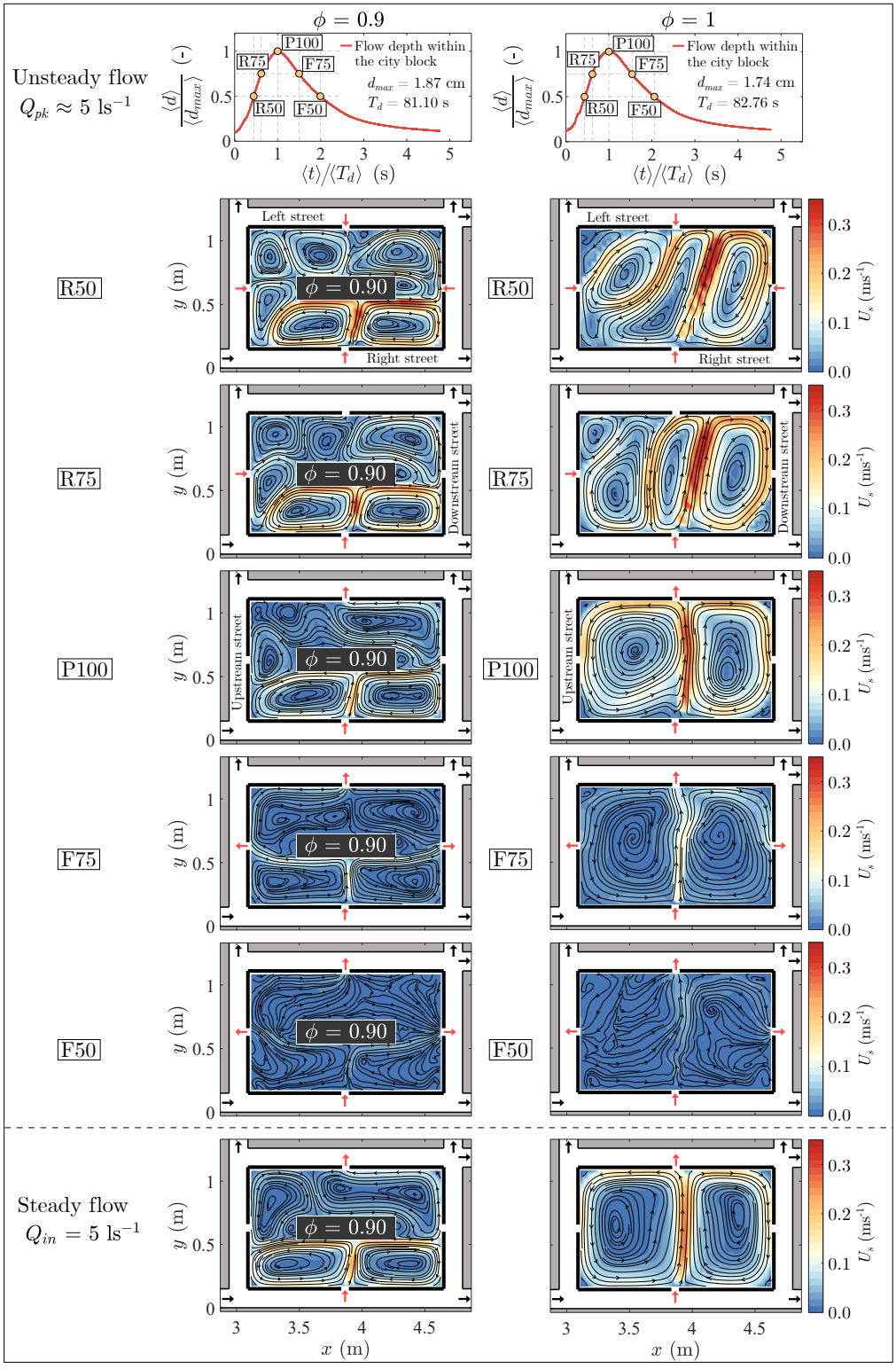

Figure 12: (Continued).

In the left street, the flow depths and particularly the velocities are lower than in the right street, therefore the risk evolves here from *low* to *moderate*. In this street, the unsteady flow hysteresis produces an accentuated difference between the rising and falling stages of the inflow hydrograph due to a backwater effect that takes place. During the rising stage, the flow from the downstream street reaches the crossroad with the left street, a backwater effect is then produced, increasing the flow depth, but not the velocity (Figure 13.b). In contrast to the right street, in this street, for a given flow depth, the level of risk is higher during the falling stage, while for a given velocity, the level of risk is higher during the rising stage.

Something important to note is that, in both right and left streets, the results for the steady flow are closer to the results for the falling stage of the inflow hydrograph, for all the various ϕ values. This might be due to the lower level of unsteadiness of the falling stage than the rising stage (see α_f and α_r values in Table 1).

The risk criterion proposed by Meja-Morales et al. (2021) was also applied to obtain 2D pedestrian flood risk maps within the city block for steady and unsteady conditions. For the unsteady flow, five risk maps are shown in Figure 14 for the cases with storage capacity (from $\phi = 0.5$ to $\phi = 1$) at the same moments as the surface velocity maps shown in section 3.4 (at d_{max} and at 50% and 75% of d_{max} in the rising and falling stages). Within the block, the highest velocities were measured during the rising stage, hence for all ϕ values, the level of risk is also higher during this stage and the risk is maximum at the maximum flood depth (P100). The level of risk varies from *low* to *significant*, being always greater in the area near the right street (because of the inflow jet, already mentioned above). A larger area with *significant* risk level is found for $\phi = 1$, because the jet through the opening in the right street is not dissipated by the interior non-porous building, and thus extends further in the block area.

The risk maps for steady flow with $Q_{in} = 5\ \mathrm{l\,s^{-1}}$ (Figure 14, bottom) slightly differ from those at d_{max} (P100) in unsteady flow. For cases $\phi = 0.5$ and $\phi = 0.75$, the risk maps for steady flow present a lower levels of risk than those for the unsteady flow while the opposite stands for case $\phi = 0.9$. For $\phi = 1$, both risk maps are very similar for steady and unsteady flows.

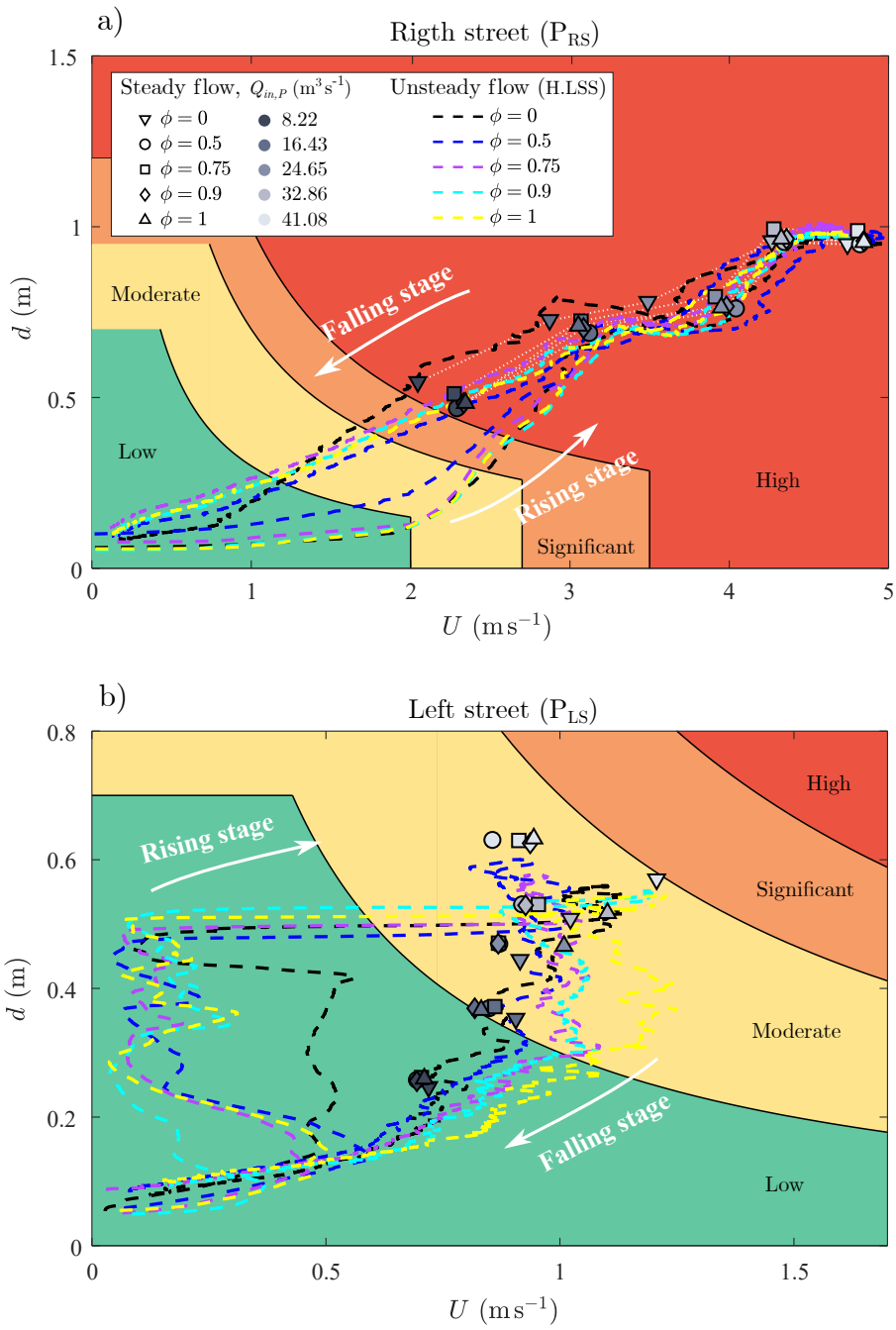

Figure 13: Curves $U_s - d$ at prototype scale in the right (a) and left (b) streets (at measuring points P_{RS} and P_{LS}, respectively), for the five storage capacity values, ϕ, plotted over the flood risk diagram for pedestrians, proposed by Mejía-Morales et al. (2021). The dashed coloured lines correspond to the unsteady flow H.LSS. The markers with grey intensity correspond to steady flows according to the inlet discharge, from $Q_{in} = 1\,l s^{-1}$ to $5\,l s^{-1}$ at model scale, here upscaled to the prototype scale.

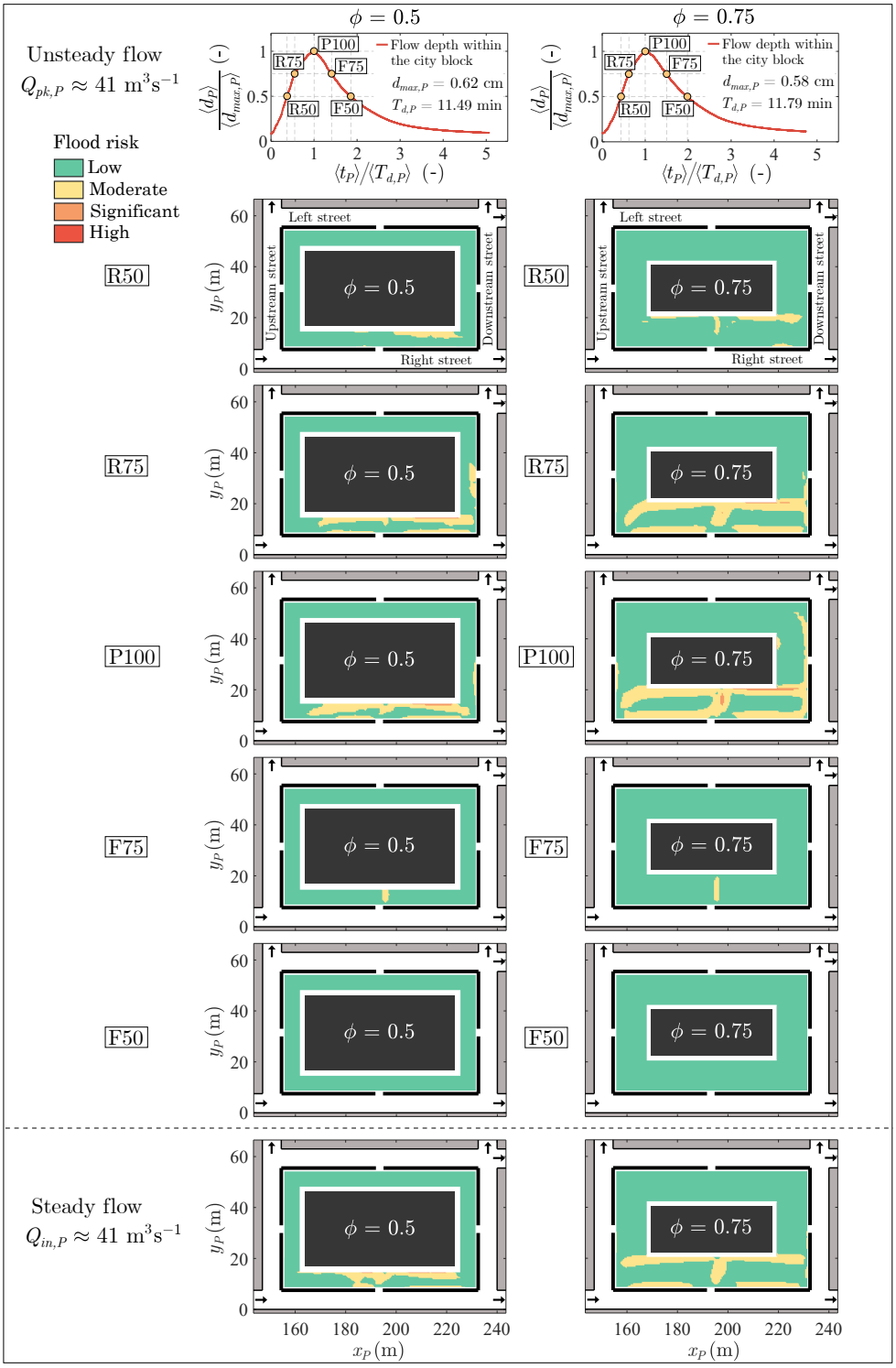

Figure 14: Flood risk maps for pedestrians at prototype scale, for cases with $\phi = 0.5,\ 0.75,\ 0.9$ and 1 during the inflow hydrograph (H.LSS): at d_{max} (P100) and at 50% and 75% of d_{max} during the rising (R50 and R75) and falling stages (F50 and F75). Flood risk maps under steady flow conditions for d_{max}, i.e. with $Q_{in} \approx Q_{pk}$ are shown at the bottom. At the top is shown the stage hydrograph, $d(t)$, within the city block, where $T_{d,P}$ is the time between the base and maximum flow depths within the city block, upscaled to the prototype scale.

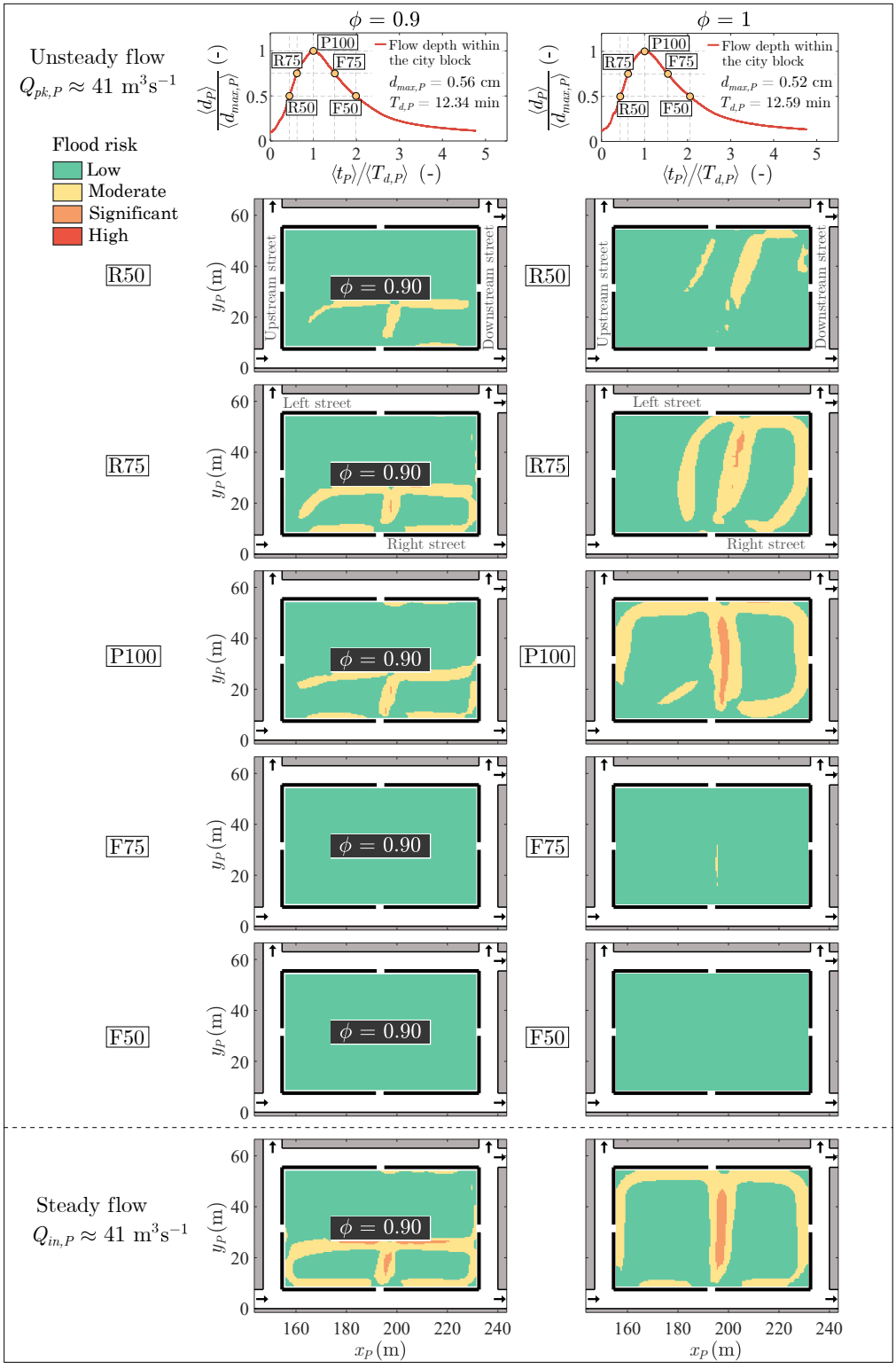

Figure 14: (Continued).

4 Discussion

In Figure 15 are shown the results corresponding to H.LSS and H.SLS (inflow hydrographs with different $V_{B,max}/V_r$ ratios), for the relative change with respect to the reference case (i.e. when $\phi = 0$), in maximum flow depth, Δd_{max} (Figure 15.a), global peak discharge, ΔQ_{pk} (Figure 15.b) and maximum surface velocity, $\Delta U_{s,max}$ (Figure 15.c) as a function of $V_{B,max}/V_r$. Plots in the right street are not included because the impact on flow depth and velocity due to floodwater volume storage within the block is marginal. For the left, upstream and downstream streets, the maximum flow depth increases (by up to 10%) when a small volume of floodwater is stored within the block (i.e., when $V_{B,max}/V_r < 10\%$), see Figure 15.a. However, when this volume increases, the flow depth is reduced, by up to -13% for $V_{B,max}/V_r \approx 18\%$, compared to the reference case. This result is consistent with the decrease in flow depth caused by the floodwater volume storage within buildings reported by Abdullah et al. (2011) and Huang et al. (2014), and the limited effect observed also by Paquier et al. (2019), all of them mentioned in Section 1.

Regarding the flow velocity in the streets, Paquier et al. (2019) reported an average 5% decrease in velocity by storing floodwater in the city blocks. However, in the present study, the flow depths and velocities strongly vary, depending on the floodwater volume stored within the city block. In the left street, the maximum velocity decreases for $V_{B,max}/V_r < 8.5\%$, with a maximum variation about -9% (Figure 15.c). For larger $V_{B,max}/V_r$ values, the maximum velocity increases respect to the reference case, by up to 10% when $V_{B,max}/V_r \approx 10\%$.

As expected, the global peak discharge decreases when the maximum volume stored within the block increases (Figure 15.b). This attenuation increases from 3% to 10% when the relative volume of floodwater stored within the block ($V_{B,max}/V_r$) increases from 6% to 18% (this is equivalent to 3.5% and 5.5% of the total volume V). These values are much lower than the ones reported by Avila et al. (2016), who obtained up to 75% when storing in tanks beneath the city blocks 17% of the total floodwater. Therefore, it is important to note that the internal spaces in the blocks can strongly modify the flood flow features, and neglecting them can lead to an underestimate of flow velocity and/or flow depth in some specific areas.

Finally, it should be noted that the intrusion and storage of floodwater into the city block requires porosity trough the block sidewalls, i.e., conveyance porosity, ψ. In this study, ψ corresponds to one opening in each of the four sidewalls, and it was kept con-

stant for all cases with a non-zero storage capacity ($\phi \neq 0$). Therefore, different conveyance porosity (different number or size of openings), different distribution of this porosity (different location of the openings on the sidewalls) and possible obstructions by urban furniture (Mignot et al., 2020) could lead to different results, but this analysis was not undertaken herein.

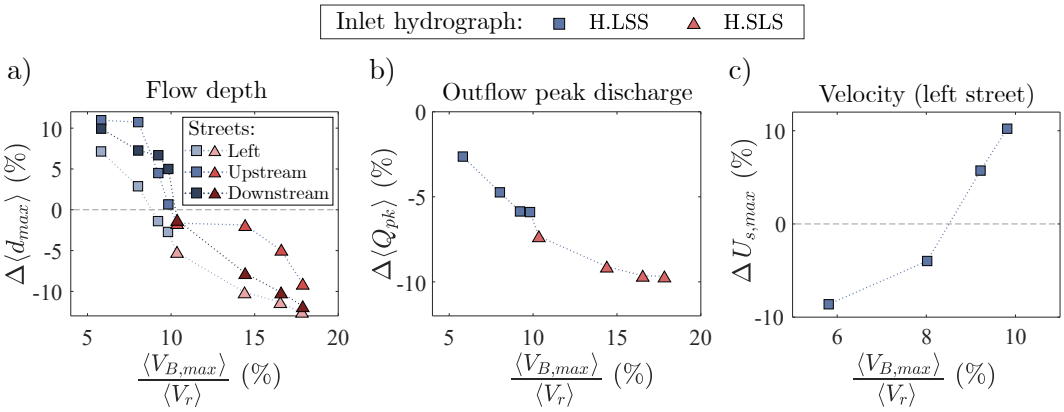

Figure 15: Relative change in maximum flow depth in left, upstream and downstream streets (a), peak discharge of global outflow hydrograph (b) and maximum surface velocity in the left street (c), respect to the reference case (i.e. when $\phi = 0$), as a function of the ratio between the floodwater volume stored within the city block, $V_{B,max}$, and the volume dispatched by the inflow hydrograph during the rising stage, V_r. Results for H.LSS and H.SLS are shown in square and triangular markers, respectively.

5 Conclusions

Relying on laboratory experiments, the present work investigates the influence of the internal space within a city block (storage capacity, ϕ) on flood flows. A simplified street network is used, with idealized street geometries and unchanged conveyance porosity along the city block, to isolate the effect on the flood risk of the varying storage volume capacity with respect to the hydrograph volume dispatched during the rising stage. Three different inflow hydrographs were considered, together with steady flows, for five storage capacity values, ϕ. For each flow case, inflow and outflow discharges were monitored, and flow depths and velocities were measured at various locations within the city block and in the streets.

It was found that increasing the storage capacity of the block, ϕ, attenuates the peak outflow discharge, with a maximum reduced peak discharge of 10%. However, ϕ can also increase the discharge in certain streets, by up to 14% in this study. Oppositely, the time lag between the inflow and global outflow hydrograph peak discharges was not significantly impacted by ϕ. The increase in storage capacity also reduced the maximum flow depth, by up to 13% for the left and downstream streets and by about 15% within the city block. The impact on the maximum surface velocity in the right street was limited to 2%, with respect to the reference case, for the maximum storage capacity. However, in the left street, the maximum surface velocity was varied, from -9% to 10%, when ϕ increased from 0.5 to 1. Finally, within the city block, a slight increase in velocity was found (7%) at the highest storage capacity value (i.e., $\phi = 1$). In this zone, where several recirculating flow cells occur, their number and size are driven by the clearance between the block walls and the non-porous building walls.

The increased storage capacity in the block causes the risk to pedestrians to increase in the left street and within the city block. Consequently, neglecting the presence of these interior spaces within city blocks during flood studies could lead to underestimate or overestimate the effects of flooding in certain areas. Therefore, it is highly advisable to take them into account together with the conveyance porosity of city blocks for a proper hazard assessment.

During these tests the influence of the inflow hydrograph unsteadiness, α_r, was quite noticeable. Among the three hydrographs tested, the results for the two hydrographs with the same α_r value (~ 2.2) were very similar and differed from those of the hydrograph with a higher unsteadiness value (H.SLS, with $\alpha_r = 4.49$). The attenuation of the global peak outflow discharge increased with increasing α_r: from 5% when $\alpha_r = 2.2$ to 10% when $\alpha_r = 4.49$. Moreover, some flood flow parameters were impacted in the opposite way when the inflow hydrograph unsteadiness level differed (e.g. maximum flow depths in some areas increased with respect to the reference case when $\alpha_r = 2.2$, whereas they decreased when $\alpha_r = 4.49$). As a result, the flood hazard (that is related to these flow parameters) and the flood risk are also variable with the inflow hydrograph unsteadiness level, which should be considered in the studies of urban floods.

The results for unsteady flows differed from those for steady flows of the same peak inflow discharge. Local flow depths were mostly greater for steady flows, by up to 30%.

The maximum surface velocity was lower in most cases for steady flows: in the left street, by up to 25% and within the city block, by up to 20%. Consequently, the assessed flood risk to pedestrians varied between steady and unsteady cases. The risk level was higher in unsteady flows for $\phi = 0.5$ and 0.75, but higher in steady flow for $\phi = 0.9$ and it was about the same for $\phi = 1$. However, the risk level for pedestrians in this study was obtained with the flood risk diagram proposed by Meja-Morales et al. (2021). It is based mainly on the people instability assessment from studies conducted in straight channels, under steady flow conditions. Therefore, instability data for people under unsteady flow conditions and in realistic urban settings would be a great improvement for better hazard assessment during flash floods in urban environments

Finally, these results are just representative of this particular simplified geometry and could change substantially in more realistic configurations of urban areas, or even with different dimensions of streets, block width-to-length ratio, slope, etc.

Open Research

The data collected in this research are available at Meja-Morales et al. (2022).

Acknowledgments

The authors acknowledge the financial support offered by the French National Research Agency (ANR) for the project DEUFI (under grant ANR-18-CE01-0020). The authors also acknowledge the technical staff at INRAE, Fabien Thollet and Adrien Bonnefoy for their valuable help in solving the various problems encountered during the experimental campaign.

References

Abdullah, A. F., Vojinovic, Z., Price, R. K., & Aziz, N. A. A. (2011). A methodology for processing raw LiDAR data to support urban flood modelling framework. *Journal of Hydroinformatics*, *14*(1), 75-92. doi: 10.2166/hydro.2011.089

Abt, S., Wittier, R., Taylor, A., & Love, D. (1989, August). Human stability in a high flood hazard zone. *Journal of the American Water Resources Association*, *25*(4), 881–890. doi: 10.1111/j.1752-1688.1989.tb05404.x

Avila, H., Avila, L., & Sisa, A. (2016). Dispersed storage as stormwater runoff

control in consolidated urban watersheds with flash flood risk. *Journal of Water Resources Planning and Management*, *142*(12), 04016056. doi: 10.1061/(ASCE)WR.1943-5452.0000702

Black, R. (1975). Flood proofing rural residences: A project agnes report. *Pennsylvania. New York State College of Agriculture and Life Sciences, Ithaca, Prepared for Economic Development Administration, Washington, DC Office of Technical Assistance*.

Bonham, A., & Hattersley, R. (1967). *Low level causeways. technical report 100.* The University of New South Wales, Water Research Laboratory, Manly Vale .

Bruwier, M., Archambeau, P., Erpicum, S., Pirotton, M., & Dewals, B. (2017). Shallow-water models with anisotropic porosity and merging for flood modelling on cartesian grids. *Journal of Hydrology*, *554*, 693-709. doi: https://doi.org/10.1016/j.jhydrol.2017.09.051

Chanson, H. (2004). *Hydraulics of open channel flow.* Elsevier.

Clausen, L., & Clark, P. (1990). The development of criteria for predicting dambreak flood damages using modelling of historical dam failures. In W. R. White (Ed.), *International Conference on River Flood Hydraulics, 17-20 Sptember 1990* (pp. 369–380). UK: John Wiley & Sons.

Cox, R., Shand, T., & Blacka, M. (2010). Australian rainfall and runoff revision project 10: appropriate safety criteria for people. *Water Research*, *978*, 085825–9454.

CRED, & UNDRR. (2020). Human cost of disasters. an overview of the last 20 years: 2000–2019. *CRED, UNDRR, Geneva*.

Dewals, B., Bruwier, M., Pirotton, M., Erpicum, S., & Archambeau, P. (2021). Porosity models for large-scale urban flood modelling: A review. *Water*, *13*(7). doi: 10.3390/w13070960

Dottori, F., & Todini, E. (2013). Testing a simple 2d hydraulic model in an urban flood experiment. *Hydrological Processes*, *27*(9), 1301-1320. doi: https://doi.org/10.1002/hyp.9370

Ferrari, A., Viero, D. P., Vacondio, R., Defina, A., & Mignosa, P. (2019). Flood inundation modeling in urbanized areas: A mesh-independent porosity approach with anisotropic friction. *Advances in Water Resources*, *125*, 98-113. doi: https://doi.org/10.1016/j.advwatres.2019.01.010

Finaud-Guyot, P., Garambois, P.-A., Araud, Q., Lawniczak, F., Franois, P., Vazquez, J., & Mos, R. (2018). Experimental insight for flood flow repartition in urban areas. *Urban Water Journal*, *15*(3), 242-250. doi: 10.1080/1573062X.2018.1433861

Gordon, A., & Stone, P. (1973). *Car stability on road floodways.* National Capital Development Commission.

Guinot, V., Sanders, B. F., & Schubert, J. E. (2017). Dual integral porosity shallow water model for urban flood modelling. *Advances in Water Resources*, *103*, 16-31. doi: https://doi.org/10.1016/j.advwatres.2017.02.009

Huang, C.-J., Hsu, M.-H., Chen, A. S., & Chiu, C.-H. (2014). Simulating the storage and the blockage effects of buildings in urban flood modeling. *Terrestrial, Atmospheric & Oceanic Sciences*, *25*(4).

Karvonen, T., Hepojoki, A., Kotala, J., & Huhta, H.-K. (2000). *The use of physical models in dam-break flood analysis, RESCDAM. final report of helsinki university of technology* (Tech. Rep.). Helsinki.

Kundzewicz, Z. W., Kanae, S., Seneviratne, S. I., Handmer, J., Nicholls, N., Peduzzi, P., ... Sherstyukov, B. (2014). Flood risk and climate change: global and regional perspectives. *Hydrological Sciences Journal*, *59*(1), 1-28. doi: 10.1080/02626667.2013.857411

Le Coz, J., Jodeau, M., Hauet, A., Marchand, B., & Le Boursicaud, R. (2014). Image-based velocity and discharge measurements in field and laboratory river engineering studies using the free fudaa-lspiv software. In *Proceedings of the international conference on fluvial hydraulics, river flow* (Vol. 3, pp. 2014–05).

Li, X., Erpicum, S., Bruwier, M., Mignot, E., Finaud-Guyot, P., Archambeau, P., ... Dewals, B. (2019, March). Technical note: Laboratory modelling of urban flooding: strengths and challenges of distorted scale models. *Hydrology and Earth System Sciences*, *23*(3), 1567–1580. doi: 10.5194/hess-23-1567-2019

Li, X., Erpicum, S., Mignot, E., Archambeau, P., Pirotton, M., & Dewals, B. (2021). Influence of urban forms on long-duration urban flooding: Laboratory experiments and computational analysis. *Journal of Hydrology*, *603*, 127034. doi: https://doi.org/10.1016/j.jhydrol.2021.127034

Meja-Morales, M. A., Mignot, E., Paquier, A., & Proust, S. (2022). *Dataset of a laboratory experiment on the effect of the storage capacity of a city block*

on unsteady urban floodwaters (version 1) [Dataset]. Recherche Data Gouv. Retrieved from `https://doi.org/10.57745/BFHGO3`

Meja-Morales, M. A., Mignot, E., Paquier, A., Sigaud, D., & Proust, S. (2021). Impact of the porosity of an urban block on the flood risk assessment: A laboratory experiment. *Journal of Hydrology*, *602*. doi: https://doi.org/10.1016/j.jhydrol.2021.126715

Mignot, E., Camusson, L., & Riviere, N. (2020). Measuring the flow intrusion towards building areas during urban floods: Impact of the obstacles located in the streets and on the facade. *Journal of Hydrology*, *583*, 124607. doi: https://doi.org/10.1016/j.jhydrol.2020.124607

Mignot, E., Li, X., & Dewals, B. (2019). Experimental modelling of urban flooding: A review. *Journal of Hydrology*, *568*, 334 - 342. doi: https://doi.org/10.1016/j.jhydrol.2018.11.001

Mignot, E., Paquier, A., & Haider, S. (2006). Modeling floods in a dense urban area using 2d shallow water equations. *Journal of Hydrology*, *327*(1), 186-199. doi: https://doi.org/10.1016/j.jhydrol.2005.11.026

Milanesi, L., Pilotti, M., Belleri, A., Marini, A., & Fuchs, S. (2018). Vulnerability to flash floods: A simplified structural model for masonry buildings. *Water Resources Research*, *54*(10), 7177-7197. doi: 10.1029/2018WR022577

Neal, J. C., Bates, P. D., Fewtrell, T. J., Hunter, N. M., Wilson, M. D., & Horritt, M. S. (2009). Distributed whole city water level measurements from the carlisle 2005 urban flood event and comparison with hydraulic model simulations. *Journal of Hydrology*, *368*(1), 42-55. doi: https://doi.org/10.1016/j.jhydrol.2009.01.026

Nezu, I., & Nakagawa, H. (1993). Basic structure of turbulence in unsteady open channel flows. In *Proc. of 9th int. symposium on turbulent shear flows, kyoto, 1993.*

Paquier, A., Bazin, P. H., & Abderrezzak, K. E. K. (2019). Sensitivity of 2d hydrodynamic modelling of urban floods to the forcing inputs: lessons from two field cases. *Urban Water Journal*, *17*(5), 457-466. doi: 10.1080/1573062X.2019.1669200

Sanders, B. F., Schubert, J. E., & Gallegos, H. A. (2008). Integral formulation of shallow-water equations with anisotropic porosity for urban flood mod-

eling. *Journal of Hydrology*, *362*(1), 19-38. doi: https://doi.org/10.1016/j.jhydrol.2008.08.009

Schubert, J. E., & Sanders, B. F. (2012). Building treatments for urban flood inundation models and implications for predictive skill and modeling efficiency. *Advances in Water Resources*, *41*, 49-64. doi: https://doi.org/10.1016/j.advwatres.2012.02.012

Shu, C., Xia, J., Falconer, R. A., & Lin, B. (2011). Incipient velocity for partially submerged vehicles in floodwaters. *Journal of Hydraulic Research*, *49*(6), 709-717. doi: 10.1080/00221686.2011.616318

Soares-Frazo, S., Lhomme, J., Guinot, V., & Zech, Y. (2008). Two-dimensional shallow-water model with porosity for urban flood modelling. *Journal of Hydraulic Research*, *46*(1), 45-64. doi: 10.1080/00221686.2008.9521842

zgen, I., Liang, D., & Hinkelmann, R. (2016). Shallow water equations with depth-dependent anisotropic porosity for subgrid-scale topography. *Applied Mathematical Modelling*, *40*(17), 7447-7473. doi: https://doi.org/10.1016/j.apm.2015.12.012